Hot and dense matter equation of state probability distributions for astrophysical simulations

Xingfu Du,[1] Andrew W. Steiner,[1,2] and Jeremy W. Holt[3]
[1]*Department of Physics and Astronomy, University of Tennessee, Knoxville, Tennessee 37996, USA*
[2]*Physics Division, Oak Ridge National Laboratory, Oak Ridge, Tennessee 37831, USA*
[3]*Cyclotron Institute and Department of Physics and Astronomy, Texas A&M University, College Station, Texas 77843, USA*

(Received 4 August 2021; revised 27 January 2022; accepted 25 February 2022; published 14 March 2022)

We add an ensemble of nuclei to the equation of state for homogeneous nucleonic matter to generate a new set of models suitable for astrophysical simulations of core-collapse supernovae and neutron star mergers. We implement empirical constraints from (i) nuclear mass measurements, (ii) proton-proton scattering phase shifts, and (iii) neutron star observations. Our model is also guided by microscopic many-body theory calculations based on realistic nuclear forces, including the zero-temperature neutron matter equation of state from quantum Monte Carlo simulations and thermal contributions to the free energy from finite-temperature many-body perturbation theory. We ensure that the parameters of our model can be varied while preserving thermodynamic consistency and the connection to experimental or observational data, thus providing a probability distribution of the astrophysical hot and dense matter equation of state. We compare our results with those obtained from other available equations of state. While our probability distributions indeed represent a large number of possible equations of state, we cannot yet claim to have fully explored all of the uncertainties, especially with regard to the structure of nuclei in the hot and dense medium.

DOI: 10.1103/PhysRevC.105.035803

I. INTRODUCTION

The equation of state (EOS) of nuclear matter is a central microscopic input for the simulation of core-collapse supernovae and neutron star mergers. In a supernova, the nuclear incompressibility generated from Fermi degeneracy pressure and short-range nuclear forces is essential in providing the pressure support which causes the infalling shockwave to "bounce" and propel the mantle off the protoneutron star underneath [1]. In a neutron star merger, the EOS determines the compactness of the two stars, which in turn determines the amount of r-process material ejected in a merger [2], the properties of the kilonova emission [3], and features of the late-inspiral gravitational wave emissions (e.g., see Ref. [4]). The EOS also determines the lifetime and final fate of the merger remnant [5–10] through the relationship between the EOS and the neutron star maximum mass.

Since weak equilibrium is not fully achieved in the short dynamical timescale of either a supernova explosion or a neutron star merger, there are at least three relevant quantities for describing the composition of dense matter: the number density of baryons n_B, the electron fraction Y_e, and the temperature T. Muons, pions, and strangeness-containing hadrons may introduce additional complexity, but as a minimal model we neglect these more exotic degrees of freedom in the present work. Simulations of supernovae or mergers which employ realistic EOSs often use tabulations that span baryon number densities $n_B \sim 10^7$–10^{15} g/cm^3, electron fractions $Y_e \sim$ 0.1–0.6, and temperatures $T \sim$ 0–100 MeV.

EOSs for core-collapse supernovae were first developed by Lattimer and Swesty [11], who employed three different nonrelativistic Skyrme effective interactions and the single-nucleus approximation to account for the presence of heavy nuclei in a gas of unbound nucleons. A second set of EOS tables was developed Shen *et al.* [12] (also using the single-nucleus approximation), which was based on the NL3 relativistic mean-field Lagrangian. While the single-nucleus approximation is sufficient to describe the bulk thermodynamics, it does not in general accurately describe the composition [13–18] and the associated weak reaction rates. Shen *et al.* [19] constructed the first full table to go beyond the single-nucleus approximation. Their work was based on a more modern relativistic mean-field model, "FSUGold" [20], and goes beyond the single nucleus approximation to include a full distribution of nuclei in nuclear statistical equilibrium (NSE). Alternative formalisms were developed by Furusawa *et al.* [21] and Hempel *et al.* [22,23], which resulted in EOS tables built upon several nucleon-nucleon interactions, including FSUGold, DD2 [24], IUFSU [25], SFHo [26], and SFHx [26]. More recently, several EOSs have been added to the CompOSE (CompStar Online Supernovae Equations of State) database [27], including an EOS with hyperons [28]. Recent EOS tables with a similar goal of matching observational and experimental constraints have been released by Schneider *et al.* [29,30].

The basic paradigm under which most EOS tables are constructed is to compute the thermodynamic quantities based on a single model of the nucleon-nucleon interaction. However,

this paradigm fails when one wants to perform *uncertainty quantification*. There is currently no model for the nucleon-nucleon interaction and the accompanying EOS which (i) faithfully describes matter in all of the density and temperature regimes which are relevant for supernovae and mergers and (ii) allows one to vary a set of parameters in such a way as to explore the uncertainties in the EOS without spoiling agreement with experiments or observations. For example, Skyrme [31] models are often used to describe dense matter for the purposes of EOS tables, but often fail to describe low-density matter as described by the virial expansion or nuclear effective field theory [32]. Even when a Skyrme effective interaction does happen to match model-independent properties of the EOS at low-densities, it does so at the cost of suppressing the uncertainties in matter at higher densities and introducing unphysical correlations between matter in the two density regimes.

Future work on the nucleon-nucleon interaction and the equation of state may eventually resolve some of these issues. In the meantime, a different approach is required to ensure that simulations can quantify the uncertainties in the EOS without over- or underconstraining the EOS. Based on our previous work in Ref. [33], we construct a phenomenological description of the free energy for hot and dense stellar matter which is able to (i) faithfully describe nuclear matter under conditions that are probed by nuclear experiments and observations of neutron stars and (ii) provides parameters which allow one to (at least partially) quantify the uncertainties which result from our imperfect knowledge of the nucleon-nucleon interaction. We add nuclei to the EOS of homogeneous nuclear matter described in Ref. [33] and show that our results compare well with other EOS tables which are available.

II. METHOD

A. Basic formalism

We use the formalism developed in Ref. [22] to describe nucleons in thermodynamic equilibrium with a distribution of nuclei. Neutrons, protons, α particles, deuterons, tritons, ^{4}Li, and ^{3}He are treated separately to more easily describe the neutrino opacities near the neutrinosphere [34]. The Helmholtz free energy density can be written as

$$f(n_n, n_p, \{n_i\}, T) = f_{np} + \sum_i f_i + f_{\rm Coul} + f_e, \tag{1}$$

where n_n and n_p are the free neutron and proton number densities, n_i is the number density of nucleus i, and $f_{\rm Coul}$ denotes the Coulomb free energy described in more detail below. We take $\hbar = c = k_B = 1$. Baryon number conservation and global charge neutrality imply two constraints, which we write as

$$\begin{aligned} n_B &= n_n + n_p + \sum_i n_i A_i, \\ n_B Y_e &= n_e = n_p + \sum_i n_i Z_i. \end{aligned} \tag{2}$$

The free energy density of nucleons outside the nucleus, denoted $f_{\rm Hom}$, is based on the homogenous nucleonic matter EOS from Ref. [33] (see discussion below). (See also Ref. [35] for an alternative EOS for homogeneous nucleonic matter). We include an excluded volume correction (which is only turned on between nucleons and nuclei), to correct for the fact that the volume available to the nucleons is reduced by the nuclei. We denote the volume available to nucleons as $V' \equiv V - \sum_i N_i V_i$, where $N_i \equiv n_i V$ is the number of nuclei of type i in the volume V, $V_i \equiv A_i/n_0$ is the volume occupied by one nucleus of type i, and n_0 is the saturation density of symmetric nuclear matter, $0.16\,{\rm fm}^{-3}$. The volume fraction that free nucleons explore is $\xi \equiv V'/V = 1 - \sum_i A_i n_i/n_0$. Thus,

$$f_{np} = \xi f_{\rm Hom}(n_n', n_p', T). \tag{3}$$

The n_n' and n_p' are local densities and are defined by $n_n' \equiv N_n/V' = n_n/\xi$, $n_p' \equiv N_p/V' = n_p/\xi$ separately. We ignore rest mass contribution here and put a tilde on top when it is added back.

The free energy density of the light nuclei and heavy nucleus are treated as classical Boltzmann particles:

$$f_i = -n_i T\left[\ln\left(\frac{\Omega_i \bar{V}}{N_i \lambda_i^3}\right) + 1\right], \tag{4}$$

where λ_i is the thermal wavelength

$$\lambda_i = \left(\frac{2\pi}{m_i T}\right)^{1/2} \tag{5}$$

and $\bar{V} \equiv \kappa V$ is the volume fraction explorable to the nucleus of type i, with $\kappa \equiv 1 - n_B/n_0$. The quantity Ω_i is the temperature-dependent partition function. The prescription we use follows from Refs. [19,36] and will be addressed in the next section. Using these definitions

$$f_i = -n_i T\left[\ln\left(\frac{\Omega_i}{n_i \lambda_i^3}\right) + 1\right] - n_i T \ln\kappa. \tag{6}$$

One can also rewrite ξ in terms of κ and the nucleon densities

$$\xi = \kappa + (n_n + n_p)/n_0 = \kappa\left(1 - \frac{n_n'}{n_0} - \frac{n_p'}{n_0}\right)^{-1}. \tag{7}$$

The Coulomb energy in the Wigner-Seitz cell is [37]

$$E_i^{\rm Coul} = -\frac{3}{5}\frac{Z_i^2 \alpha}{R_i}\left(\frac{3}{2}x_i - \frac{1}{2}x_i^3\right), \tag{8}$$

where

$$x_i \equiv \left(\frac{n_B Y_e}{n_0}\frac{A_i}{Z_i}\right)^{1/3} = \frac{R_i}{R_{{\rm WS},i}}, \tag{9}$$

where $R_i^3 = (3A_i)/(4\pi n_0)$ is the nuclear radius and the size of the Wigner-Seitz cell, $R_{\rm WS}$, is given by

$$Z_i = \frac{4\pi}{3} R_{{\rm WS},i}^3 n_B Y_e. \tag{10}$$

The radius of nuclei is constrained by $R_i \leqslant R_{{\rm ws},i}$ which limits $x_i \leqslant 1$.

We take into account all charged particles here except protons, the advantage is the Coulomb energy is merely a function of charge and atomic number given n_B and Y_e.

After applying charge neutrality, the total free energy density becomes

$$f(n_n, n_p, \{n_i\}, T) = \xi f_{\rm Hom}(n_n', n_p', T) - \sum_i n_i T \left\{ \left[\ln\left(\frac{\Omega_i}{n_i \lambda_i^3}\right) + 1 \right] + \ln \kappa \right\} + \sum_i n_i E_i^{\rm Coul} + f_e(n_B Y_e). \quad (11)$$

B. Homogeneous matter

We slightly modify the EOS of homogeneous matter from Ref. [33] to no longer enforce a quadratic expansion for the isospin-asymmetry dependence of the finite-temperature contributions. The free energy is separated into a contribution from the virial expansion and a contribution from degenerate matter:

$$f_{\rm Hom}(n_B, x_p, T) = f_{\rm virial}(n_B, x_p, T) g + f_{\rm deg}(n_B, x_p, T)(1-g). \quad (12)$$

The free energy density for degenerate matter is

$$f_{\rm deg}(n_B, x_p, T) = f_{\rm Skyrme}(n_B, x_p = 1/2, T = 0) + \delta^2 \varepsilon_{\rm sym}(n_B) + \Delta f_{\rm hot}(n_B, x_p, T). \quad (13)$$

Based on the work in Ref. [38], most of our tables use the Skyrme model labeled SKχm* to compute $\Delta f_{\rm hot}$. This Skyrme model was fitted to the equation of state of asymmetric nuclear matter [39,40] calculated from several realistic chiral two- and three-body forces as well as consistent nucleon isoscalar and isovector effective masses derived from the nucleon self-energy [41,42]. In particular, the description of nuclear matter thermal properties relies on accurately modeling the nucleon effective mass, which is proportional to the density of states near the Fermi surface and hence the temperature dependence of the entropy [43,44]. We also construct two tables with alternative models for $\Delta f_{\rm hot}$, Skχ414 and Skχ450 from Ref. [45]. The derivatives of the degenerate free energy density are

$$\frac{\partial f_{\rm deg}}{\partial n_n} = \frac{1}{2}\mu_{n,\rm Skyrme}(n_B, x_p = 1/2, T = 0) + \frac{1}{2}\mu_{p,\rm Skyrme}(n_B, x_p = 1/2, T = 0) + \delta^2 \frac{\partial \varepsilon_{\rm sym}}{\partial n_B} + \frac{2\delta(1-\delta)}{n_B}\varepsilon_{\rm sym} + \Delta\mu_{n,\rm hot}(n_B, x_p, T), \quad (14)$$

$$\frac{\partial f_{\rm deg}}{\partial n_p} = \frac{1}{2}\mu_{p,\rm Skyrme}(n_B, x_p = 1/2, T = 0) + \frac{1}{2}\mu_{n,\rm Skyrme}(n_B, x_p = 1/2, T = 0) + \delta^2 \frac{\partial \varepsilon_{\rm sym}}{\partial n_B} - \frac{2\delta(1+\delta)}{n_B}\varepsilon_{\rm sym} + \Delta\mu_{p,\rm hot}(n_B, x_p, T), \quad (15)$$

and

$$\frac{\partial f_{\rm deg}}{\partial T} = -s_{\rm hot}(n_B, x_p, T), \quad (16)$$

where

$$\frac{\partial \varepsilon_{\rm sym}}{\partial n_B} = h'(n_B)\varepsilon_{\rm QMC}(n_B) + h(n_B)\varepsilon'_{\rm QMC}(n_B) - h'(n_B)\varepsilon_{\rm NS}(n_B) + [1-h(n_B)]\varepsilon'_{\rm NS}(n_B) - \frac{1}{2}[\mu_{n,\rm Skyrme}(n_B, x_p = 1/2, T = 0) + \mu_{p,\rm Skyrme}(n_B, x_p = 1/2, T = 0)]. \quad (17)$$

In Eq. (17), the auxiliary function h' is used to interpolate between the pure neutron matter equation of state $\varepsilon_{\rm QMC}$ valid around normal nuclear densities and the high-density equation of state $\varepsilon_{\rm NS}$ that may be constrained by neutron star observations. Note that $\varepsilon_{\rm QMC}$ is given by the quantum Monte Carlo inspired form

$$\varepsilon_{\rm QMC} = n_B \left[a\left(\frac{n_B}{n_0}\right)^\alpha + b\left(\frac{n_B}{n_0}\right)^\beta \right]. \quad (18)$$

C. The Saha equations

In order to fix the densities of the nuclei, we solve the equations

$$\left(\frac{\partial f}{\partial n_i}\right)_{n_B, Y_e} = 0. \quad (19)$$

Before we begin, it is useful to define

$$f_{i,\rm Cl} = -n_i T \left[\ln\left(\frac{\Omega_i}{n_i \lambda_i^3}\right) + 1 \right] \quad (20)$$

as the classical part of the nuclear free energy.

We can rewrite the full free energy from Eq. (11) in terms of n_B and Y_e:

$$f[n_n(n_B, Y_e, T), n_p(n_B, Y_e, T), \{n_i\}, T], \quad (21)$$

to re-express the derivative (T is implicitly held constant),

$$\left(\frac{\partial f}{\partial n_i}\right)_{n_B, Y_e} = \left(\frac{\partial f}{\partial n_i}\right)_{n_p, n_n} + \left(\frac{\partial f}{\partial n_n}\right)_{n_p, \{n_i\}} \left(\frac{\partial n_n}{\partial n_i}\right)_{n_B, Y_e} + \left(\frac{\partial f}{\partial n_p}\right)_{n_n, \{n_i\}} \left(\frac{\partial n_p}{\partial n_i}\right)_{n_B, Y_e} = \left(\frac{\partial f}{\partial n_i}\right)_{n_p, n_n} - \left(\frac{\partial f}{\partial n_n}\right)_{n_p, \{n_i\}} N_i - \left(\frac{\partial f}{\partial n_p}\right)_{n_n, \{n_i\}} Z_i. \quad (22)$$

Thus, we obtain the Saha equations

$$\mu_i = \mu_n N_i + \mu_p Z_i \quad (23)$$

with the chemical potentials denoted by

$$\mu_i \equiv \left(\frac{\partial f}{\partial n_i}\right)_{n_p, n_n, T}, \quad \mu_n \equiv \left(\frac{\partial f}{\partial n_n}\right)_{n_p, \{n_i\}, T}, \quad \text{and} \quad \mu_p \equiv \left(\frac{\partial f}{\partial n_p}\right)_{n_n, \{n_i\}, T}. \quad (24)$$

We also define $\mu_e \equiv (\partial f_e)/(\partial n_e)$. Note that our formalism naturally implies that the chemical potential of the neutrons and protons inside nuclei is the same as that outside nuclei (i.e., the neutrons and protons are in chemical equilibrium). To see this how this works for neutrons, use Eq. (23) for $i = (Z, N+1)$ and $i = (Z, N)$ and then subtract, giving

$$\mu_{(Z,N+1)} - \mu_{(Z,N)} = (N+1)\mu_n - N\mu_n = \mu_n. \tag{25}$$

In particular, the reaction $(Z, N+1) \leftrightarrow (Z, N) + n$ is in equilibrium. The same reasoning applies equally well to protons.

These chemical potentials can be written analytically. For the nuclei, we define

$$P_i^{\rm Coul} \equiv -n_i \frac{3}{5}\frac{Z_i^2\alpha}{R_i}\left(\frac{1}{2}x_i - \frac{1}{2}x_i^3\right) \tag{26}$$

as in Ref. [22] and this definition implies

$$n_i\left(\frac{\partial E_i^{\rm Coul}}{\partial n_i}\right)_{n_n,n_p} = \frac{P_i^{\rm Coul} Z_i}{n_e}. \tag{27}$$

For the nuclei, this definition gives

$$\begin{aligned}\mu_i = &-\left(\frac{A_i}{n_0}\right) f_{\rm Hom} + \mu_{n,{\rm Hom}}\left(\frac{A_i n_n}{\xi n_0}\right) + \mu_{p,{\rm Hom}}\left(\frac{A_i n_p}{\xi n_0}\right)\\ &+ \mu_{i,{\rm cl}} - T\ln\kappa + \frac{T n_i A_i}{\kappa n_0} + E_i^{\rm Coul}\\ &+ \frac{Z_i P_i^{\rm Coul}}{n_e} + Z_i\mu_e,\end{aligned} \tag{28}$$

where $\mu_{i,{\rm cl}} \equiv (\partial f_{i,{\rm cl}})/(\partial n_i)$. For the nucleons

$$\mu_n = \mu_{n,{\rm Hom}} + \frac{T n_i}{\kappa n_0} \tag{29}$$

and

$$\mu_p = \mu_{p,{\rm Hom}} + \frac{T n_i}{\kappa n_0} + \mu_e + \frac{P^{\rm Coul}}{n_e}, \tag{30}$$

where $\mu_{x,{\rm Hom}} \equiv (\partial f_{\rm Hom})/(\partial n_x)$ and $P^{\rm Coul} \equiv \sum_i P_i^{\rm Coul}$. Note that because we have not included electrons as separate degrees of freedom in Eq. (11), the electron chemical potential appears in Eq. (30). Thus, our chemical potentials above match those in Ref. [22]. Using the Saha equation, we find

$$\begin{aligned}\mu_{i,{\rm cl}} = &\left(\frac{A_i}{n_0}\right) f_{\rm Hom} + \mu_{n,{\rm Hom}}\left[N_i - \left(\frac{A_i n_n}{\xi n_0}\right)\right]\\ &+ \mu_{p,{\rm Hom}}\left[Z_i - \left(\frac{A_i n_p}{\xi n_0}\right)\right] + T\ln\kappa - E_i^{\rm Coul},\end{aligned} \tag{31}$$

which gives us a recipe for computing the free energy for each nucleus. Using $P_{\rm Hom} \equiv -f_{\rm Hom} + \mu_{n,{\rm Hom}} n_n' + \mu_{p,{\rm Hom}} n_p'$, we can rewrite this result slightly

$$\mu_{i,{\rm cl}} = -V_i P_{\rm Hom} + N_i\mu_{n,{\rm Hom}} + Z_i\mu_{p,{\rm Hom}} + T\ln\kappa - E_i^{\rm Coul}. \tag{32}$$

The excluded volume effect reflected in the $T\ln\kappa$ and $-P_{\rm Hom}V_i$ terms suppresses the number density of nuclei near saturation densities. Note that, because we are able to compute the chemical potentials in Eqs. (28)–(30) analytically, our derivation of the Saha equations includes the rearrangement terms described in Ref. [46]. Of course, this simple excluded volume approximation which we use is not sufficient for accurately mimicking the multicomponent plasma at low-temperature (for example, we cannot use this model to accurately measure the crystallization temperature) but is a reasonable approximation for the high-temperature environment encountered in supernovae and neutron star mergers.

At a fixed grid point in (n_B, Y_e, T) space, given n_n and n_p, we can compute κ and ξ using their definitions above, compute the homogeneous matter EOS and $E_i^{\rm Coul}$ and thus use Eq. (32) to compute $\mu_{i,{\rm cl}}$. This is then used to compute n_i and then we can solve Eqs. (2) to obtain the correct value of n_n and n_p. Internally, our code defines $x_n \equiv n_n'/n_0$ and $x_p \equiv n_p'/n_0$ and then solves Eqs. (2) in terms of the variables $\log_{10} x_n$ and $\log_{10} x_p$.

The solution of Eqs. (2) is not unique because of the liquid-gas phase transition and the discrete nature of the nuclei in the distribution, so we often use neighboring points as initial guesses and choose the solution that minimizes the free energy. Our solver automatically decreases the step size when unphysical configurations are encountered, but occasionally it does not converge, especially just below the nuclear saturation density. Note that our method implies a small discontinuity in the free energy at the liquid-gas phase transition, but our previous experience in simulations based on SFHo and SHFx [26] shows that this small discontinuity is not typically an issue in core-collapse and merger simulations.

We approach this with a combination of techniques, all of which are automatically applied until a solution is found: (i) iteratively solving for neutron and proton conservation separately using a bracketing method (ii) using a minimizer instead of a solver and (iii) restarting the solver with random initial points near the initial guess.

D. First derivatives

After having solved the Saha equations for $n_i(n_n, n_p)$, it is useful to define new "effective" chemical potentials for the nucleons which include the nucleons both inside and outside nuclei

$$\nu_n \equiv \left(\frac{\partial f}{\partial n_n}\right)_{n_p,T} \quad \text{and} \quad \nu_p \equiv \left(\frac{\partial f}{\partial n_p}\right)_{n_n,T} \tag{33}$$

[note that these differ from Eq. (24) in that they no longer hold n_i constant] which gives a new thermodynamic identity

$$f(n_n, n_p, T) = -P(n_n, n_p, T) + \nu_n n_n + \nu_p n_p. \tag{34}$$

Rewriting the free energy again

$$f[n_n, n_p, \{n_i(n_n, n_p, T)\}, T], \tag{35}$$

which implies that the effective chemical potentials can be computed in terms of the definitions above

$$\nu_x = \mu_x + \sum_i \mu_i\left(\frac{\partial n_i}{\partial n_x}\right)_{n_{\hat{x}}} \tag{36}$$

for both $\{x, \hat{x}\} = \{n, p\}$ and $\{x, \hat{x}\} = \{p, n\}$. Defining

$$g_j \equiv \mu_j - \mu_n N_j - \mu_p Z_j, \tag{37}$$

we can take advantage of the fact that all the g_j are constant to write

$$\left(\frac{\partial n_i}{\partial n_x}\right)_{n_{\hat{x}},g_j} = -\left(\frac{\partial g_i}{\partial n_x}\right)_{n_i,n_{\hat{x}},g_{j\neq i}} \left(\frac{\partial n_i}{\partial g_i}\right)_{n_x,n_{\hat{x}},g_{j\neq i}}. \tag{38}$$

The first derivative on the RHS can be obtained directly from Eqs. (28)–(30). The second derivative is just an element along the diagonal of the inverse of the matrix

$$M_{ij} \equiv \left(\frac{\partial g_i}{\partial n_j}\right)_{n_x,n_{\hat{x}},n_{k\neq j}}. \tag{39}$$

The numerical errors associated with inverting this large matrix decreases the benefit of the analytical formalism. Thus we compute ν_n and ν_p numerically for now. The entropy is easier to compute

$$s = -\left(\frac{\partial f}{\partial T}\right)_{n_n,n_p,\{n_i\}} = s_e + \sum_i s_i + \sum_i n_i \ln\kappa + \xi s_{\rm Hom}, \tag{40}$$

where $s_e = \partial f_e/\partial T$ and

$$s_i = n_i\left(\ln\frac{\Omega_i}{n_i\lambda_i^3}\right) + \frac{5}{2} + \frac{T}{\Omega_i}\frac{d\Omega_i}{dT}. \tag{41}$$

E. Nuclei

We use the nuclear masses from experiment [47] wherever they are available. The atomic mass tables usually include an empirical bounded electron contribution term $a_{el}Z^{2.39}$, which is subtracted before the binding energy is calculated. We use the theoretical masses from Ref. [48] for nuclei which do not have experimental mass measurements up to the neutron and proton drip lines. We use the experimental or theoretical spins tabulated in Ref. [49]. Finally, we limit $Z < 7N$ and $N < 7Z$ in order to avoid extreme nuclei which our model likely does not describe well.

F. Partition function

The partition function we use for light nuclei and the representative heavy nucleus follows from Ref. [19]. The nuclear partition function can be expressed as a sum of discrete states and an integral of the level density

$$\Omega_i = (2J+1) + \int_{E_d}^{E_t} \rho(E)\exp(-E/T), \tag{42}$$

where the level density $\rho(E)$ is the back-shifted Fermi-gas formula given below. The limits on the integral in the partition function are determined from

$$E_d = \tfrac{1}{2}\min(S_n, S_p) \quad \text{and} \tag{43}$$

$$E_t = \min\left(S_n + E_R, S_p + E_R + \tfrac{1}{2}E_c\right), \tag{44}$$

where S_n and S_p are the neutron and proton separation energies. The quantity $E_R \equiv 1/(2M_iR^2)$ is the zero-point energy and with the nuclear radius approximated by $R = 1.25\,\text{fm}\,(A-1)^{1/3}$. The Coulomb barrier is $E_c \equiv (Z-1)\alpha/R$. When either S_n or S_p is negative, the contribution of the level density to the partition function is neglected.

The expression for the level density begins by defining a back-shift parameter δ for each nucleus. The prescription from Ref. [36] is

$$Z \leqslant 30 : \delta = \delta_p - 80/A, \tag{45}$$

$$Z \geqslant 30 : \delta = \delta_p - 80/A - 0.5 \tag{46}$$

with $\delta_p = (11A^{-1/2}\,\text{MeV})[1 + (1/2)(-1)^Z + 1/2(-1)^N]$. We will also need the level density parameter, a, for which an approximate model is

$$Z \leqslant 30 : a = 0.052\,\text{MeV}^{-1}\,A^{1.2}, \tag{47}$$

$$Z \geqslant 30 : a = 0.125\,\text{MeV}^{-1}\,A. \tag{48}$$

Finally, different expressions are used for the level density depending on the relative size of δ and E_d. When δ is smaller than E_d, the level density has the expression

$$\rho(E) = \frac{\pi}{12}\frac{\exp(2\sqrt{aU})}{a^{1/4}U^{5/4}}, \tag{49}$$

where $U = E - \delta$.

When δ is larger than E_d, δ is set to E_d (so that $U = E - E_d$) and the level density is

$$\rho(E) = C\exp(U/T_c), \tag{50}$$

where

$$\frac{1}{T_c} = \frac{5}{4}\frac{1}{\delta} + \frac{\sqrt{a}}{\sqrt{\delta}}, \text{ and} \tag{51}$$

$$C = \frac{\sqrt{\pi}}{12}a^{-1/4}\delta^{-5/4}\exp\left(\frac{5}{4} + \sqrt{a\delta}\right).$$

The derivative of the partition function with respect to the temperature is required for computing the entropy [see Eq. (41)], and this is straightforward to compute analytically.

This recipe for the partition function is only approximate and underestimates the contribution from excited states [50,51]. Reference [19] found that this approximation did not adversely impact the thermodynamics of dense matter, but a more systematic and quantitative exploration of these uncertainties is an important avenue for future work.

III. RESULTS

While our EOS formalism is designed to be used for any physical values of the parameters, we precompute nine tables and present results based on those parametrizations. The parameters $\{i_{\rm NS}, i_{\rm Skyrme}, \alpha, a, L(\text{MeV}), S(\text{MeV}), \phi\}$ are (i) the choice of high-density EOS parametrization selected from a discrete set of Markov-chain samples constructed in Ref. [52], (ii) the choice of Skyrme effective interaction selected from 1000 samples generated from the posterior probability distribution in Ref. [53], (iii and iv) the power and prefactor in Eq. (18) for the neutron matter equation of state, (v and vi) the symmetry energy slope parameter, the symmetry energy, and (vii) the speed of sound at the largest density we consider, $n_B = 2\,\text{fm}^{-3}$. Reference [33] uses the Skyrme EOS for isospin-symmetric matter, but has a separate parameters for the symmetry energy parameters S and L to describe neutron

TABLE I. Parameters for the EOS tables generated for this work. The model with note 1 was constructed with the Skχ414 model for $\Delta f_{\rm hot}$ from Ref. [45], and the model with note 2 was constructed with the Skχ450 model for $\Delta f_{\rm hot}$ from Ref. [45].

	$i_{\rm NS}$	$i_{\rm Skyrme}$	α	a	L (MeV)	S (MeV)	ϕ
fiducial	470	738	0.5	13.0	62.4	32.8	0.9
large $M_{\rm max}$	783	738	0.5	13.0	62.4	32.8	0.9
small R	214	738	0.5	13.0	62.4	32.8	0.9
smaller R	256	738	0.5	13.0	62.4	32.8	0.9
large R	0	738	0.5	13.0	62.4	32.8	0.9
small SL	470	738	0.5	13.0	23.7	29.5	0.9
large SL	470	738	0.5	13.0	100.0	36.0	0.9
fiducial[1]	470	738	0.5	13.0	62.4	32.8	0.9
fiducial[2]	470	738	0.5	13.0	62.4	32.8	0.9

matter. The Skyrme models are calibrated to experimental nuclear properties which constrain nuclear isospin-symmetric matter well but do not accurately constrain neutron matter. For this reason, Ref. [33] uses quantum Monte Carlo calculations from Ref. [54] to constrain neutron matter and thus the values of S and L. The parameters of the nine equation of state tables are listed in Table I. The finite temperature corrections are determined by a separate Skyrme model which is calibrated to finite-temperature many-body calculations from Ref. [45]. The principal uncertainty in these calculations is the choice of the momentum cutoff, so we choose a range of values, from 414 MeV to 450 MeV Ref. [45] to quantify this uncertainty. The fiducial EOS is consistent with the most probable neutron star mass and radius while having moderate S and L (see details in Ref. [33]). The Skyrme parameters for our fiducial EOS are listed in Table II. In the following, the figures are demonstrated for our fiducial EOS.

A. Composition of hot and dense matter

In Fig. 1, the baryon number fraction of free neutrons, protons, light nuclei, and heavy nuclei are plotted as a function of baryon density for $Y_e = 0.1$ and $Y_e = 0.5$. The baryon number fraction of species i is

$$X_i \equiv n_i A_i / n_B, \tag{52}$$

where n_i is the number per unit volume for species i and A_i is the number of baryons in species i. Equation (2) ensures

TABLE II. Parameters for Skyrme Hamiltonian $i_{\rm Skyrme} = 738$.

t_0	-2719.7 MeV fm^3
t_1	417.64 MeV fm^5
t_2	-66.687 MeV fm^5
t_3	15042 MeV fm$^{3(1+\epsilon)}$
x_0	0.16154
x_1	-0.047986
x_2	0.027170
x_3	0.13611
ϵ	0.14416

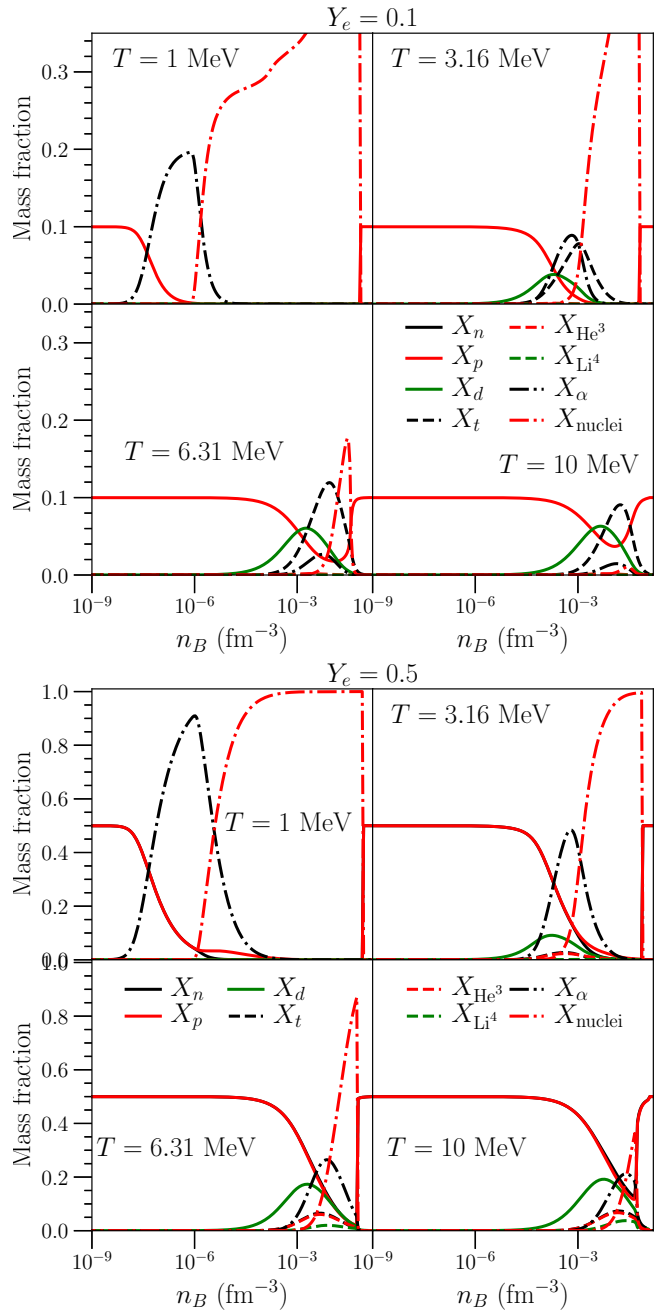

FIG. 1. Baryon number fractions X_i for protons, light nuclei, and a sum over heavy nuclei, as a function of density for $Y_e = 0.1$ and $Y_e = 0.5$ for four temperatures. In the top four panels, the neutron baryon number fraction is omitted to help make the heavy nuclei more visible. In the bottom four panels, the neutron mass fraction is hidden behind the proton mass fraction at low densities where these two quantities coincide. The right edge of the plots is chosen to be $n_B = n_0$ and nuclei always disappear at a baryon density below n_0 (independent of electron fraction or temperature).

$\sum_i X_i = 1$. The quantity $X_{\rm nuclei}$ is defined by

$$X_{\rm nuclei} \equiv 1 - X_n - X_p - X_d - X_t - X_\alpha - X_{^3{\rm He}} - X_{^4{\rm Li}}. \tag{53}$$

At low densities, the system consists of only protons and neutrons. For $Y_e = 0.1$ and $T = 1.0$ MeV, as density increases,

the mass fraction of alpha particles rises to around 0.2 for n_B between 10^{-7} and $10^{-6}\,\mathrm{fm}^{-3}$. Above $10^{-6}\,\mathrm{fm}^{-3}$, the light nuclei are gradually replaced by heavy nuclei. The transition density from light to heavy nuclei increases as temperature increases. For $Y_e = 0.5$, α particles are even more prominent at lower densities and heavier nuclei dominate more strongly near the transition to nucleonic matter. For higher temperature (but independent of electron fraction), the region of light and heavy nuclei gradually merge to a single peak.

Figure 2 shows baryon number fractions X_n, X_p and Fig. 3 shows baryon number fractions X_α, X_{nuclei} as a function of baryon density and temperature. Near $Y_e = 0.5$ and at low temperatures, the system consists almost entirely of heavy nuclei. As the temperature increases, the nonuniform clusters transform to uniform matter. On the other hand, as Y_e decreases, nuclei are replaced by free neutrons. The critical temperature of the gas-liquid phase transition is around several to tens of MeV depending on the proton fraction.

To compute the average proton and neutron number of nuclei, we define

$$\bar{Z} = \left(\sum_i Z_i n_i\right)\left(\sum_i n_i\right)^{-1}, \tag{54}$$

where this sum includes the light nuclei d, t, α, ^{3}He, and ^{4}Li. We define a similar quantity $\bar{N}$, and the average nuclear mass number is then $\bar{A} \equiv \bar{N} + \bar{Z}$. Figure 4 shows $\bar{A}$ and $\bar{Z}$ as a function of baryon density and temperature. The maximum A for our EOS is limited to about 340. For symmetric nuclear matter, $\bar{A}$ reaches the upper limit we set. For smaller electron fractions, the maximum mass number decreases to 120 as neutrons leave nuclei to form a gas. The shell structure of nuclei is evident in the figures as rapid color changes. As baryon density increases, $\bar{A}$ rises to several plateaus. Figure 5 shows the charge and mass number of nuclei as a function of density and electron fraction at four fixed temperatures. The transition density from inhomogeneous matter to homogeneous matter is not independent of proton fraction, as observed in microscopic calculations of the equation of state [40,55]. The transition density is largest near $Y_e \approx 0.4$, which is to be expected since heavy laboratory nuclei have a similar proton fraction. At higher temperatures nuclei disappear as we approach the liquid gas transition.

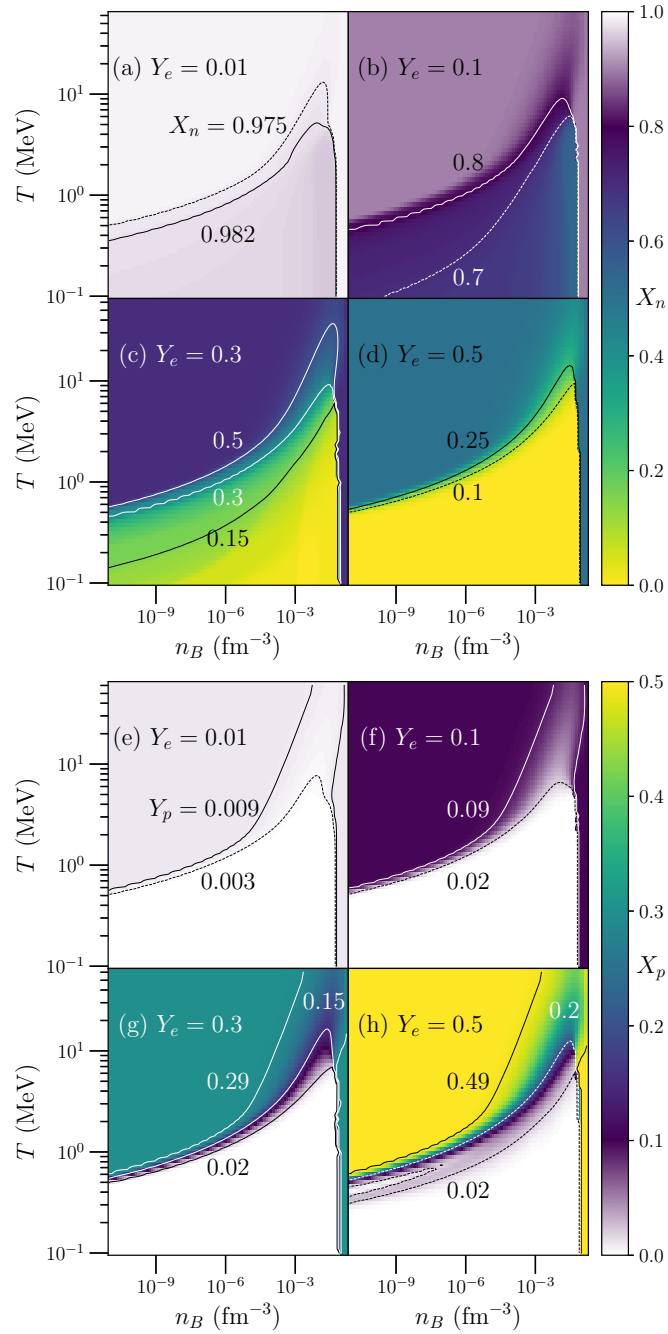

FIG. 2. Baryon number fractions X_n and X_p as a function of baryon density and temperature for $Y_e = 0.01$, 0.1, 0.3, 0.5, respectively. The right edge of the plots is chosen to be $n_B = n_0$ where nuclei disappear (independent of electron fraction or temperature).

B. Comparison with other EOSs

Figure 6 shows the average mass number A as a function of baryon density and temperature for several other EOSs: LS220 [11], SFHO [26], FSU21 [56], NRAPR [29], STOS [12], and FYSS [21]. Note that these results were interpolated from the files created by Ref. [57] (and stored at `stellarcollapse.org`), and thus details may differ slightly from the original files. Significant differences can be found among these plots for the predictions of mass number in inhomogeneous phase. The plots fall into two categories. STOS, FSU21, and FYSS allow nuclei with maximum mass number around several thousand, while LS220, NRAPR and SFHo limit A below several hundred. There is also some variation between models in the Y_e dependence of the phase transition between nuclei and nuclear matter. In FSU21 and FYSS, the phase transition is nearly Y_e independent. Note that different panels have different maximum values of Y_e, and this impacts the apparent shape of the transition to nucleonic matter. The STOS, FSU21, and FYSS tables all include a pasta phase before transitioning to homogeneous matter, and this also complicates the comparison. The inclusion of the pasta phase, in general, decreases binding energy and therefore favors a late transition to homogeneous matter. Note however that the

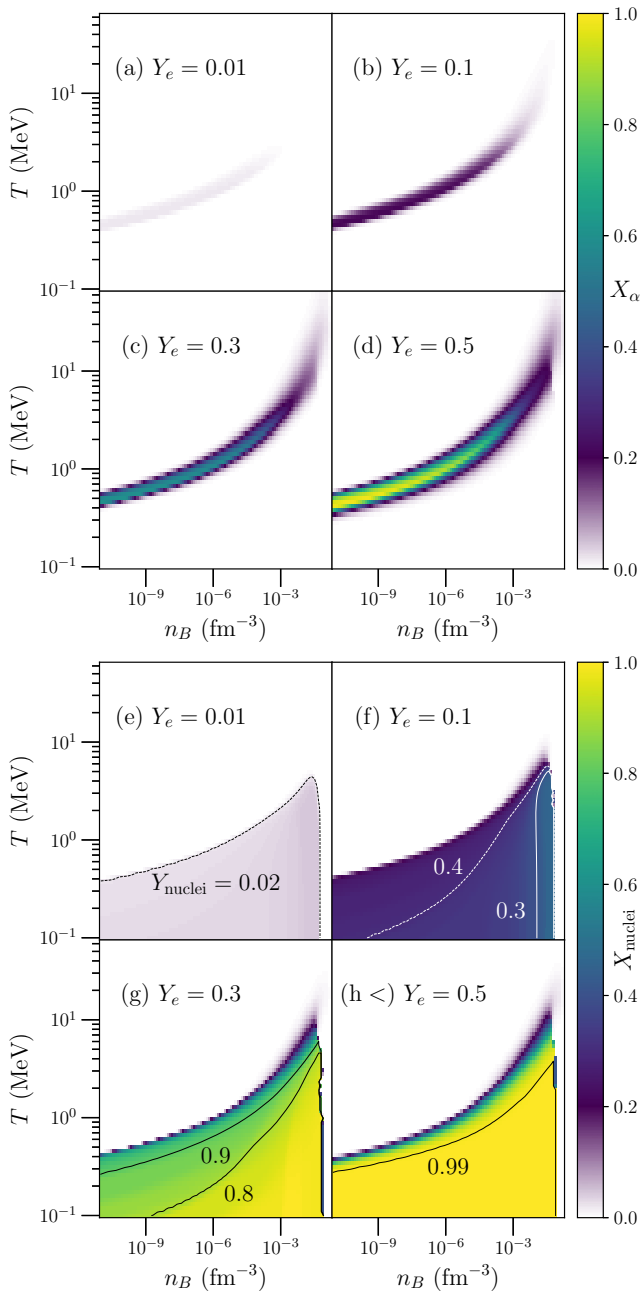

FIG. 3. Baryon number fractions X_α and $X_{\rm nuclei}$ as a function of baryon density and temperature for $Y_e = 0.01, 0.1, 0.3, 0.5$, respectively. The right edge of the plots is chosen to be $n_B = n_0$ where nuclei disappear (independent of electron fraction or temperature).

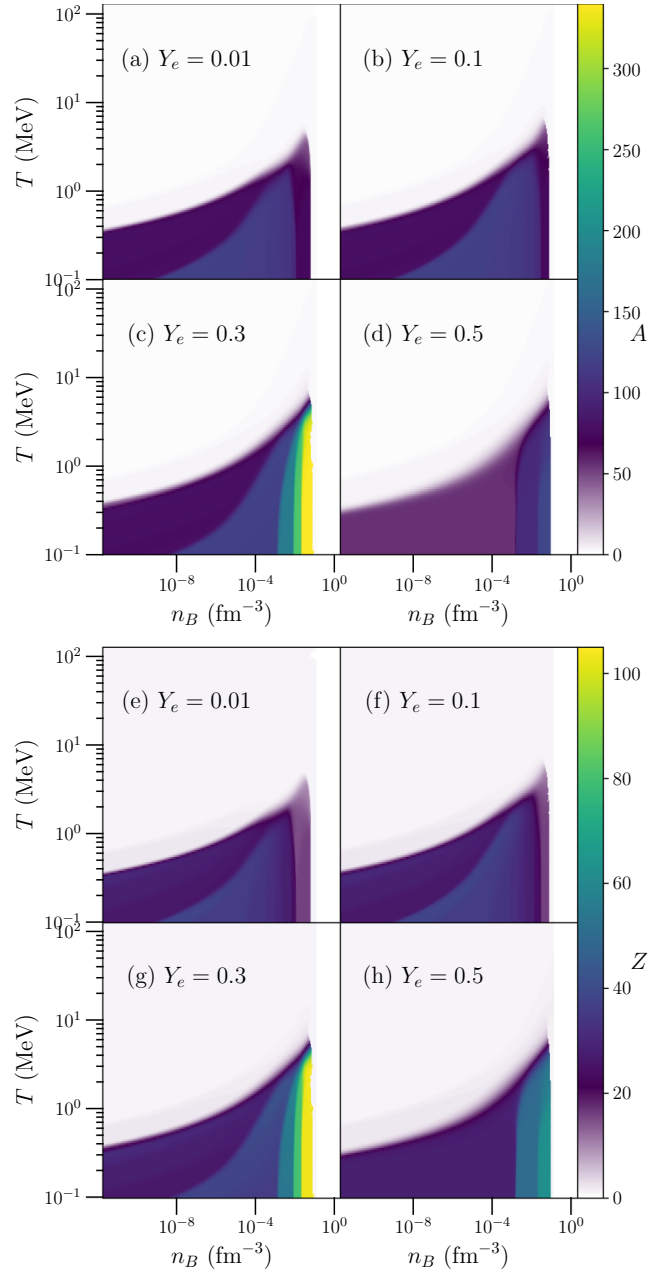

FIG. 4. Average mass(top)/proton(bottom) number for $Y_e = 0.01, 0.1, 0.3, 0.5$, respectively.

difference of the mass number between EOS tables does not strongly impact the thermodynamic quantities such as the pressure and entropy [13].

C. Nuclear distribution

Figure 7 shows the nuclear distribution for selected points in the EOS as in [19]. Our results are similar, and our restriction of $Z < 7N$ and $N < 7Z$ is evident in the linear cutoff in the distribution near the lower-left corner in each panel. A significant number of nuclei participate in the EOS at each point. Even though we do not fully explore this uncertainty in this work, we find that changing the distribution can significantly change the transition to nucleonic matter. This variation may impact core-collapse supernovae and protoneutron star evolution, as implied by the recent discussion in Ref. [58]. Figure 8 shows the isotopic distribution for the same four points in the (n_B, Y_e, T) space. The distribution shows a structure created by the magic numbers (peaks near $Z = 28$ and $Z = 50$ are evident), as well as a peak at low Z as found earlier in Ref. [18].

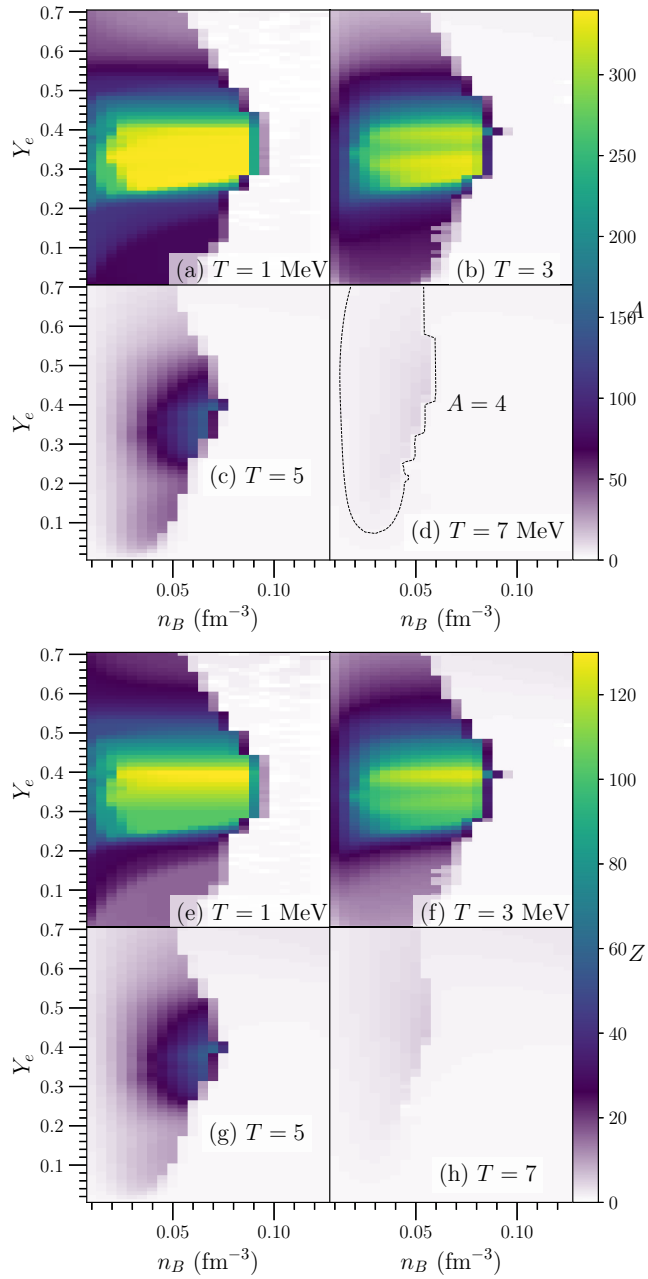

FIG. 5. Average mass (top four panels) and proton (bottom four panels) number for $T = 1, 3, 5, 7$ MeV, respectively.

D. Monte Carlo results

Figure 9 shows four Monte Carlo plots of the average mass number for some selected points when the seven parameters in our EOS are randomly selected. The distribution gives uncertainty of the EOS in subnuclear density at low temperature at four points where the distribution is nearly maximal. The distribution of A is wider at extreme values of Y_e, the top panels show results for $Y_e = 0.05$ and $Y_e = 0.65$. The bottom-left panel shows that the probability distribution is particularly wide for larger densities near the transition to nucleonic matter in large part because heavy nuclei are present in some models but not others. This effect persists even up to large densities, as shown in the lower-right panel, where nuclei are present for some models but not others. At the large proton fractions represented by the lower-right panel, large nuclei are excluded from being present due to the small inter-nuclear spacing. The uncertainty in the nucleon-nucleon interaction then leads to some models with a significant number of α particles and other light nuclei (right peak) and a few models with no nuclei at all (left peak).

At some points in the (n_B, Y_e, T) space, the variation shown in Fig. 9 is much smaller than the variation between other EOS tables. At $n_B = 0.03\,\mathrm{fm}^{-3}$, $Y_e = 0.05$, and $T = 5$ MeV (corresponding to the upper-left panel of Fig. 9), LS220 gives $A = 9$ but STOS gives $A = 204$ whereas our result is 19.5 ± 3.5. Our variation in some regions, however, is larger than the variation between EOS tables. At $n_B = 0.08\,\mathrm{fm}^{-3}$, $Y_e = 0.05$, and $T = 1$ MeV (corresponding to the lower-left panel of Fig. 9), NRAPR gives $A = 1$, FSU21 gives $A = 0$, FYSS gives $A = 12$, LS220 gives $A = 4$, SFHO gives $A = 1$, and STOS gives $A = 0.15$, while our result is as large as $A = 45$ for some parametrizations.

IV. DISCUSSION

While we have created a code which can propagate the uncertainties in the nucleon-nucleon interaction to the resulting equation of state, we have not yet fully included all of the uncertainties. In particular, in addition to the several uncertainties which are involved in the calculation of homogeneous nucleonic matter (discussed in Ref. [33]), there are several additional uncertainties involving nuclei which we have not included. Pasta structures, which are present to surprisingly large temperatures [58,59], are not included in the present work. In addition, the modification of the nuclear surface energy due to the presence of nucleons outside nuclei (see, e.g., Refs. [60,61]) has not been included in this work. While these corrections are principally important at lower temperatures, and are thus subleading, they may impact the resulting nuclear distribution, particularly in core-collapse supernovae.

We also do not include all of the possible nuclear many-body effects. For example, we do not yet include nuclei beyond the driplines, as it would significantly increase the size of the distribution of nuclei which we have to consider at every point in the (n_B, Y_e, T) space. However, these nuclei can impact the final composition [62,63]. In addition, we do not yet use the same underlying nucleon-nucleon interaction for both homogeneous matter and nuclei, and Ref. [64] has shown that this inconsistency may result in spurious effects in the composition. We have not found an impact on the composition in the tables which we have generated, but we cannot yet fully rule this out.

One important consideration is the recent experimental measurement of a large value for L, as measured in PREX-II [65,66]. While our fiducial model has a smaller value of L one of our alternate parametrizations has a value of $L = 100$ MeV, only 6 MeV away from the central value suggested in Ref. [66].

The nucleon effective mass has been recently shown to be particularly important for both core-collapse supernovae and mergers [67,68]. While the parametrizations tabulated

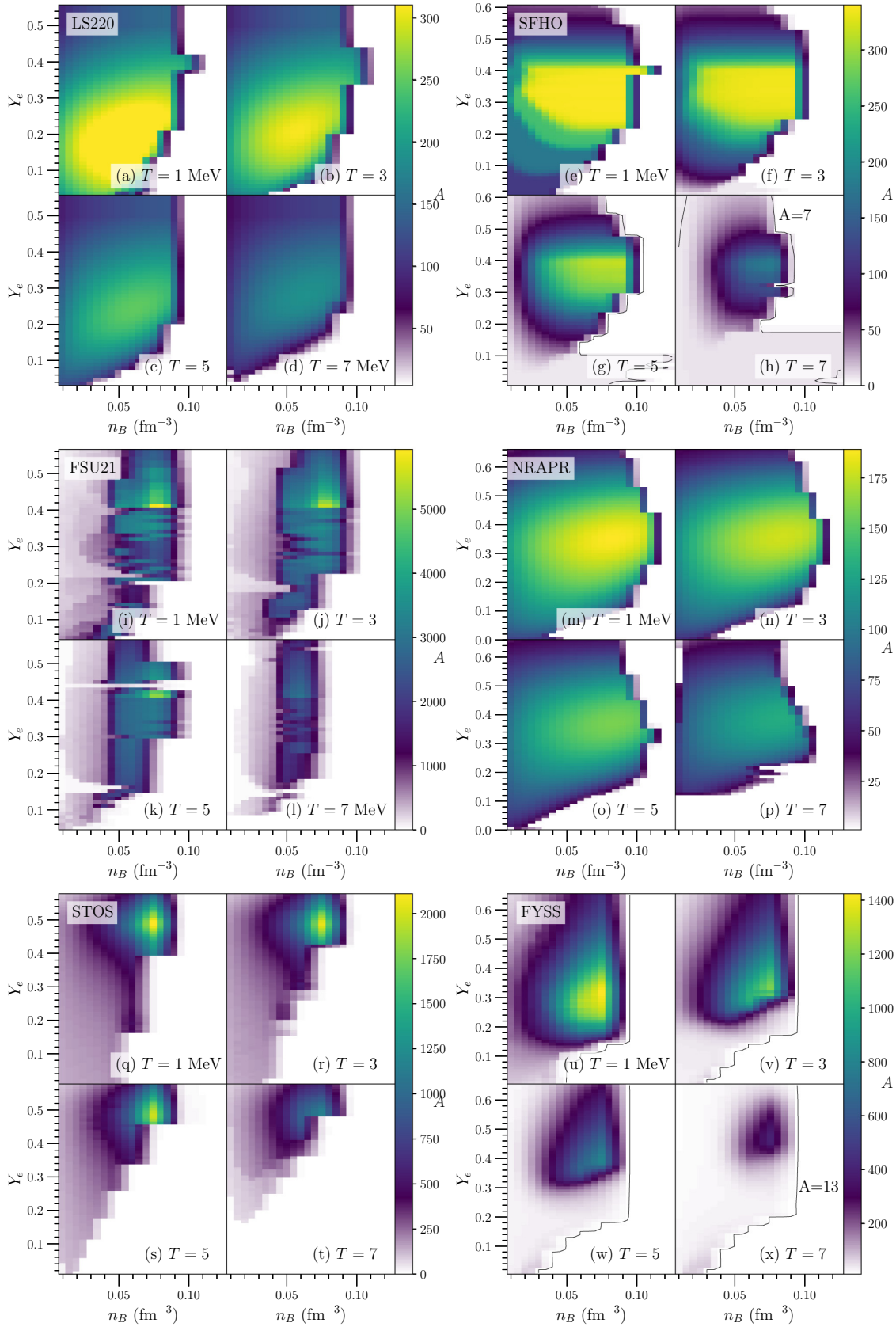

FIG. 6. Average mass number for $T = 1$, 3, 5, and 7 MeV, for the LS220, SFHO, FSU21, NRAPR, STOS, and FYSS EOSs.

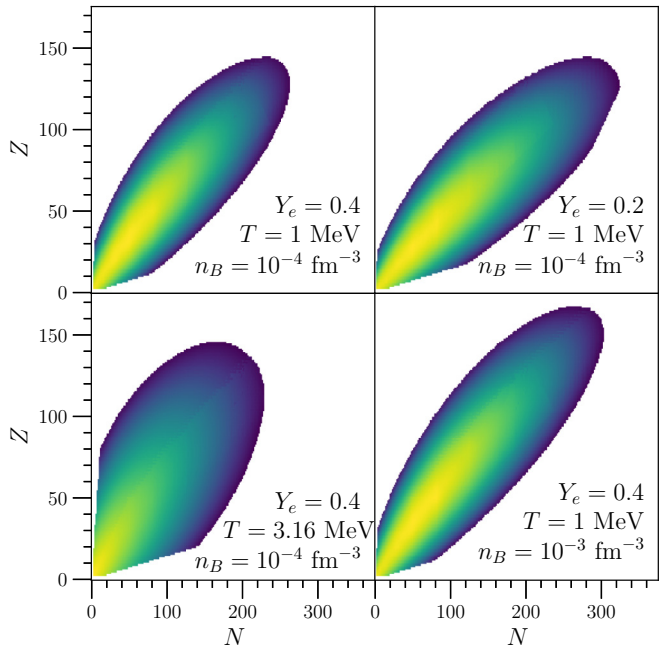

FIG. 7. Mass fraction of nuclei in the nuclear chart for matter at four selected points, comparable with Ref. [19].

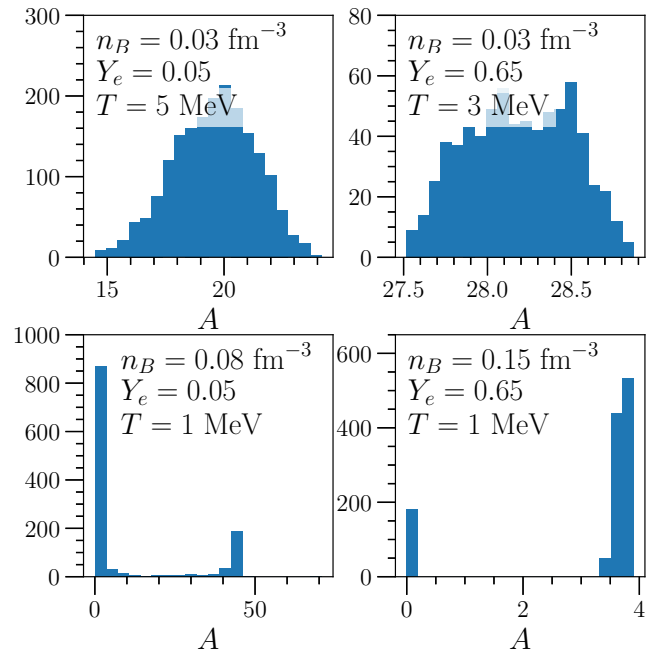

FIG. 9. Probability distribution for the average nuclear mass number for equations of state generated by our code at four points.

in Table I all use the same Skyrme model (which has a reduced effective mass of 0.904), the zero temperature effective masses are indeed modified in our full Monte Carlo results presented in Fig. 9. We do not vary the finite-temperature effective mass from our Skyrme model, SKχm*, because we do not yet have a probability distribution for the finite temperature part of the EOS, but this work is in progress. The effective mass, unlike the equation of state, is not a quantum mechanical observable (it depends, for example, on the arbitrary demarcation between the kinetic and potential energy). Thus it only has a unique specification in the context of a particular model or class of models. However, the effective mass is important for computing the neutrino mean free path, which is well-defined, and clearly relevant for simulations of supernovae and mergers. Thus the best way to properly assess the impact of the effective mass is construct a probability distribution of *both* the equation of state and the neutrino opacities together. Work on this direction is also in progress.

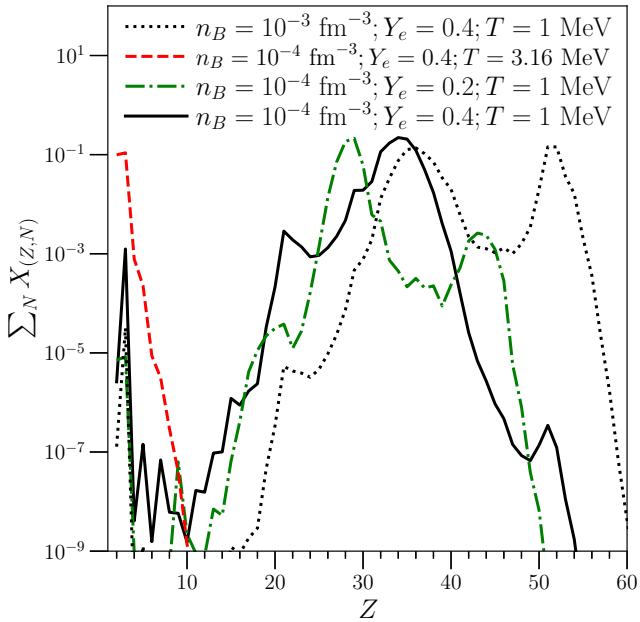

FIG. 8. Isotopic distribution for the same four points shown in Fig. 7.

The open-source code for this work, [69], is built upon O2scl [70], GSL, HDF5, and matplotlib [71]. The tables are available for download at [72].

ACKNOWLEDGMENTS

The authors thank Zidu Lin and the anonymous referee for helpful comments. The work of X.D. and A.W.S. was supported by DOE SciDAC Grant No. DE-SC0018232 and the DOE Office of Nuclear Physics. The work of J.W.H. is supported by the National Science Foundation under Grant No. PHY1652199. This research used resources of the National Energy Research Scientific Computing Center (NERSC), a U.S. Department of Energy Office of Science User Facility located at Lawrence Berkeley National Laboratory, operated under Contract No. DE-AC02-05CH11231.

[1] H. A. Bethe, G. E. Brown, J. Applegate, and J. M. Lattimer, Nucl. Phys. A **324**, 487 (1979).
[2] Y. Sekiguchi, K. Kiuchi, K. Kyutoku, and M. Shibata, Phys. Rev. D **91**, 064059 (2015).
[3] D. Kasen, B. Metzger, J. Barnes, E. Quataert, and E. Ramirez-Ruiz, Nature (London) **551**, 80 (2017).
[4] T. Hinderer, Astrophys. J. **677**, 1216 (2008).
[5] A. Bauswein, O. Just, H.-T. Janka, and N. Stergioulas, Astrophys. J. Lett. **850**, L34 (2017).
[6] B. Margalit and B. D. Metzger, Astrophys. J. Lett. **850**, L19 (2017).
[7] D. Radice, A. Perego, F. Zappa, and S. Bernuzzi, Astrophys. J. Lett. **852**, L29 (2018).
[8] L. Rezzolla, E. R. Most, and L. R. Weih, Astrophys. J. Lett. **852**, L25 (2018).
[9] M. Ruiz, S. L. Shapiro, and A. Tsokaros, Phys. Rev. D **97**, 021501(R) (2018).
[10] M. Shibata, S. Fujibayashi, K. Hotokezaka, K. Kiuchi, K. Kyutoku, Y. Sekiguchi, and M. Tanaka, Phys. Rev. D **96**, 123012 (2017).
[11] J. M. Lattimer and F. D. Swesty, Nucl. Phys. A **535**, 331 (1991).
[12] H. Shen, H. Toki, K. Oyamatsu, and K. Sumiyoshi, Nucl. Phys. A **637**, 435 (1998).
[13] A. Burrows and J. M. Lattimer, Astrophys. J. **285**, 294 (1984).
[14] W. R. Hix, O. E. B. Messer, A. Mezzacappa, M. Liebendörfer, J. Sampaio, K. Langanke, D. J. Dean, and G. Martinez-Pinedo, Phys. Rev. Lett. **91**, 201102 (2003).
[15] A. S. Botvina and I. N. Mishustin, Phys. Rev. C **72**, 048801 (2005).
[16] E. O'Connor, D. Gazit, C. J. Horowitz, A. Schwenk, and N. Barnea, Phys. Rev. C **75**, 055803 (2007).
[17] A. Arcones, G. Martinez-Pinedo, E. O'Connor, A. Schwenk, H.-T. Janka, C. J. Horowitz, and K. Langanke, Phys. Rev. C **78**, 015806 (2008).
[18] S. R. Souza, A. W. Steiner, W. G. Lynch, R. Donangelo, and M. A. Famiano, Astrophys. J. **707**, 1495 (2009).
[19] G. Shen, C. J. Horowitz, and S. Teige, Phys. Rev. C **82**, 045802 (2010).
[20] B. G. Todd-Rutel and J. Piekarewicz, Phys. Rev. Lett. **95**, 122501 (2005).
[21] S. Furusawa, S. Yamada, K. Sumiyoshi, and H. Suzuki, Astrophys. J. **738**, 178 (2011).
[22] M. Hempel and J. Schaffner-Bielich, Nucl. Phys. A **837**, 210 (2010).
[23] M. Hempel, T. Fischer, J. Schaffner-Bielich, and M. Liebendörfer, Astrophys. J. **748**, 70 (2012).
[24] S. Typel, G. Röpke, T. Klähn, D. Blaschke, and H. H. Wolter, Phys. Rev. C **81**, 015803 (2010).
[25] F. J. Fattoyev, C. J. Horowitz, J. Piekarewicz, and G. Shen, Phys. Rev. C **82**, 055803 (2010).
[26] A. W. Steiner, M. Hempel, and T. Fischer, Astrophys. J. **774**, 17 (2013).
[27] S. Typel, M. Oertel, and T. Klaehn, arXiv:1307.5715 (2013), http://compose.obspm.fr/.
[28] S. Banik, M. Hempel, and D. Bandyopadhyay, Astrophys. J. Suppl. Ser. **214**, 22 (2014).
[29] A. S. Schneider, L. F. Roberts, C. D. Ott, and E. O'Connor, Phys. Rev. C **100**, 055802 (2019).
[30] A. S. Schneider, C. Constantinou, B. Muccioli, and M. Prakash, Phys. Rev. C **100**, 025803 (2019).
[31] T. H. R. Skyrme, Nucl. Phys. **9**, 615 (1959).
[32] T. Krüger, I. Tews, K. Hebeler, and A. Schwenk, Phys. Rev. C **88**, 025802 (2013).
[33] X. Du, A. W. Steiner, and J. W. Holt, Phys. Rev. C **99**, 025803 (2019).
[34] C. J. Horowitz, G. Shen, E. O'Connor, and C. D. Ott, Phys. Rev. C **86**, 065806 (2012).
[35] S. Huth, C. Wellenhofer, and A. Schwenk, Phys. Rev. C **103**, 025803 (2021).
[36] W. A. Fowler, C. A. Engelbrecht, and S. E. Woosley, Astrophys. J. **226**, 984 (1978).
[37] G. Baym, C. Pethick, and P. Sutherland, Astrophys. J. **170**, 299 (1971).
[38] Z. Zhang, Y. Lim, J. W. Holt, and C. M. Ko, Phys. Lett. B **777**, 73 (2018).
[39] F. Sammarruca, L. Coraggio, J. W. Holt, N. Itaco, R. Machleidt, and L. E. Marcucci, Phys. Rev. C **91**, 054311 (2015).
[40] C. Wellenhofer, J. W. Holt, and N. Kaiser, Phys. Rev. C **92**, 015801 (2015).
[41] J. W. Holt, N. Kaiser, G. A. Miller, and W. Weise, Phys. Rev. C **88**, 024614 (2013).
[42] J. W. Holt, N. Kaiser, and G. A. Miller, Phys. Rev. C **93**, 064603 (2016).
[43] C. Constantinou, B. Muccioli, M. Prakash, and J. M. Lattimer, Phys. Rev. C **89**, 065802 (2014).
[44] E. Rrapaj, A. Roggero, and J. W. Holt, Phys. Rev. C **93**, 065801 (2016).
[45] Y. Lim and J. W. Holt, Phys. Rev. C **95**, 065805 (2017).
[46] T. Carreau, A. F. Fantina, and F. Gulminelli, Astron. Astrophys. **640**, A77 (2020).
[47] G. Audi, M. Wang, A. Wapstra, F. Kondev, M. MacCormick, X. Xu, and B. Pfeiffer, Chin. Phys. C **36**, 1287 (2012).
[48] P. Möller, J. R. Nix, W. D. Myers, and W. J. Swiatecki, At. Data Nucl. Data Tables **59**, 185 (1995).
[49] S. Goriely, M. Samyn, and J. M. Pearson, Phys. Rev. C **75**, 064312 (2007).
[50] D. L. Tubbs and S. E. Koonin, Astrophys. J. Lett. **232**, L59 (1979).
[51] P. Bonche, S. Levit, and D. Vautherin, Nucl. Phys. A **427**, 278 (1984).
[52] A. W. Steiner, S. Gandolfi, F. J. Fattoyev, and W. G. Newton, Phys. Rev. C **91**, 015804 (2015).
[53] M. Kortelainen, J. McDonnell, W. Nazarewicz, E. Olsen, P.-G. Reinhard, J. Sarich, N. Schunck, S. M. Wild, D. Davesne, J. Erler, and A. Pastore, Phys. Rev. C **89**, 054314 (2014).
[54] S. Gandolfi, J. Carlson, and S. Reddy, Phys. Rev. C **85**, 032801(R) (2012).
[55] S. Fiorilla, N. Kaiser, and W. Weise, Nucl. Phys. A **880**, 65 (2012).
[56] G. Shen, C. J. Horowitz, and E. O'Connor, Phys. Rev. C **83**, 065808 (2011).
[57] E. O'Connor and C. D. Ott, Classical and Quantum Gravity **27**, 114103 (2010).
[58] A. Roggero, J. Margueron, L. F. Roberts, and S. Reddy, Phys. Rev. C **97**, 045804 (2018).
[59] H. Pais, W. G. Newton, and J. R. Stone, Phys. Rev. C **90**, 065802 (2014).
[60] J. M. Lattimer, C. J. Pethick, D. G. Ravenhall, and D. Q. Lamb, Nucl. Phys. A **432**, 646 (1985).
[61] A. W. Steiner, M. Prakash, J. M. Lattimer, and P. J. Ellis, Phys. Rep. **411**, 325 (2005).

[62] A. Raduta and F. Gulminelli, Nucl. Phys. A **983**, 252 (2019).
[63] G. Röpke, Phys. Rev. C **101**, 064310 (2020).
[64] G. Grams, S. Giraud, A. F. Fantina, and F. Gulminelli, Phys. Rev. C **97**, 035807 (2018).
[65] D. Adhikari, H. Albataineh, D. Androic, K. Aniol, D. S. Armstrong, T. Averett, C. Ayerbe Gayoso, S. Barcus, V. Bellini, R. S. Beminiwattha *et al.* (PREX Collaboration), Phys. Rev. Lett. **126**, 172502 (2021).
[66] B. T. Reed, F. J. Fattoyev, C. J. Horowitz, and J. Piekarewicz, Phys. Rev. Lett. **126**, 172503 (2021).
[67] O. E. Andersen, S. Zha, A. da Silva Schneider, A. Betranhandy, S. M. Couch, and E. P. O'Connor, Astrophys. J. **923**, 201 (2021).
[68] C. Raithel, V. Paschalidis, and F. Özel, Phys. Rev. D **104**, 063016 (2021).
[69] https://github.com/awsteiner/eos.
[70] A. W. Steiner, O2scl: Object-oriented scientific computing library (2014), Astrophysics Source Code Library, record ascl:1408.019, http://ascl.net/1408.019.
[71] J. D. Hunter, Comput. Sci. Eng. **9**, 90 (2007).
[72] https://neutronstars.utk.edu/code/eos.